Edward Y. Lee
Editor

Mark C. Liszewski
Michael S. Gee
Pedro Daltro
Associate Editors

Ricardo Restrepo
Associate Imaging Editor

Pediatric Body MRI

A Comprehensive, Multidisciplinary Guide

Springer

Pediatric Body MRI

Edward Y. Lee, MD, MPH
Editor

Mark C. Liszewski, MD
Michael S. Gee, MD, PhD
Pedro Daltro, MD, PhD
Associate Editors

Ricardo Restrepo, MD
Associate Imaging Editor

Heron Werner Junior, MD, PhD
Assistant Imaging Editor

Pediatric Body MRI

A Comprehensive, Multidisciplinary Guide

Springer

Editor
Edward Y. Lee, MD, MPH
Division of Thoracic Imaging
Department of Radiology
Boston Children's Hospital
Harvard Medical School
Boston, MA, USA

Associate Editors
Mark C. Liszewski, MD
Division of Pediatric Radiology
Departments of Radiology and Pediatrics
The Children's Hospital at Montefiore and
Montefiore Medical Center Bronx,
New York, NY, USA

Pedro Daltro, MD, PhD
Alta Excelência Diagnóstica and
Department of Radiology
Clínica Diagnóstico por Imagem (CDPI)
Rio de Janeiro, Brazil

Michael S. Gee, MD, PhD
Division of Pediatric Imaging
Department of Radiology
Massachusetts General Hospital
Harvard Medical School
Boston, MA, USA

Ricardo Restrepo, MD
Department of Interventional Radiology
and Body Imaging
Nicklaus Children's Hospital
Miami, FL, USA

Assistant Imaging Editor
Heron Werner Junior, MD, PhD
Alta Excelência Diagnóstica and
Department of Radiology
Clínica Diagnóstico por Imagem (CDPI)
Rio de Janeiro, Brazil

ISBN 978-3-030-31988-5 ISBN 978-3-030-31989-2 (eBook)
https://doi.org/10.1007/978-3-030-31989-2

This Springer imprint is published by the registered company Springer Nature Switzerland AG
The registered company address is: Gewerbestrasse 11, 6330 Cham, Switzerland

To my parents, Kang-Ja and Kwan-Pyo, for instilling in me the values of hard work and dedication
To my family for their constant support, love, and encouragement
To my editorial team for contributing their time and expertise in this project. There is absolutely no better group to be with

Edward Y. Lee, MD, MPH

To my supportive wife, Jiwon, and our wonderful children, James and Emily
To my loving parents, Kathleen and Steven

Mark C. Liszewski, MD

To my parents, Elizabeth and Stanley, and my brother Brian, for their love and support

Michael S. Gee, MD, PhD

To my family, especially to my wife Leise and to my four kids, Pedro, João, Maria and Isabel
To the my pediatric radiology team, with whom I have proudly been working for so many years

Pedro Daltro, MD, PhD

To my parents, Jairo and Helena, for providing the inspiration that guided me throughout my career
To LBS for his support and for constantly reminding me that life is beautiful and to be enjoyed in all aspects

Ricardo Restrepo, MD

To my family for their constant support, love, and encouragement

Herone Werner Junior, MD, PhD

Preface

Ever since its first development approximately four decades ago, MR imaging has undergone rapid growth and technological advancement in screening, diagnosis, and follow-up assessment of various medical disorders. Particularly in recent years, the advancement to 3T and 7T magnets combined with many newer and faster MR imaging sequences and multichannel coils with parallel imaging capabilities has substantially improved the quality of MR imaging and allowed 3D imaging while reducing imaging acquisition time. In addition, due to its many advantages, including lack of harmful ionizing radiation, superb soft tissue characterization, and capacity to obtain functional information, MR imaging is currently being increasingly utilized as an integral component of noninvasive imaging assessment in many clinical circumstances in the pediatric population. Therefore, a clear understanding of pediatric MR imaging techniques and characteristic MR imaging findings of various pediatric disorders is essential for practicing pediatric and general radiologists, who encounter pediatric patients in their clinical practice to ensure optimal pediatric patient care.

The initial idea of this book arose from trainees, pediatric radiologists, general radiologists, and various specialists whom I have encountered as a pediatric radiologist at Boston Children's Hospital, chair of the pediatric radiology section of the Core Examination for radiology residents and Online Longitudinal Assessment (OLA) Committee for practicing pediatric radiologists at the American Board of Radiology (ABR), and visiting professor to more than 50 different countries around the world for the past 15 years. Everyone from these groups was looking for an up-to-date single volume practical resource for learning and reviewing the fundamentals and essentials of pediatric body MR imaging. However, there was no such book currently available. From this came my desire to write a pediatric body MR imaging textbook.

This book is organized into 17 main chapters based on organ systems in addition to a last chapter dedicated to whole body MR imaging. The organization and presentation of this book are structured to provide accessibility to both common and less common but clinically important pediatric body disorders that can be currently evaluated with MR imaging. Each chapter included in this book is designed to provide up-to-date information on current as well as emerging MR imaging techniques and outline methods to specifically tailor MR imaging for each individual pediatric patient. Practical strategies including pre-imaging pediatric patient preparation are highlighted. Developmental embryology, normal anatomy and variants, and characteristic MR imaging findings are reviewed. In addition, the discussion of each disorder includes the clinical features, characteristic MR imaging findings, and up-to-date management information in some selected cases. Given its focus on disorders affecting the pediatric population, we have emphasized how to differentiate between normal variants and abnormal pathology and how to determine whether certain MR imaging findings are related to age or a genetic or malformation syndrome. Furthermore, current information on optimizing performance, analysis, and interpretation of MR imaging is highlighted along with practical tips on navigating technical and interpretative pitfalls that occur in pediatric body MR imaging.

This book is intended primarily for radiology trainees and practicing pediatric and general radiologists. However, other physicians in different specialties as well as MR technologists and physicists who encounter the pediatric patient for MR imaging may derive valuable clini-

cal MR imaging and some patient management information that can be used to optimize their pediatric patient care.

For a book such as this one, which requires an extensive collaborative effort for preparation, I am a strong believer that we are only as good as the people that we work with. This book has greatly benefited from the tireless work of gifted associate and assistant editors whom I can proudly call my true "academic brothers." No word can adequately thank associate editors, Mark C. Liszewski, Michael S. Gee, and Pedro Daltro, for sharing their boundless enthusiasm and depth of knowledge in pediatric disorders. I am especially appreciative of Ricardo Restrepo, image associate editor, and Heron Werner Junior, image assistant editor, for their careful attention to detail in image acquisition and preparation. I would also like to thank the contributing authors of this book for their superb work, all of whom are experts or rising stars in the field of pediatric body MR imaging. Lastly but also importantly, I would like to acknowledge Margaret Moore and her colleagues at Springer for understanding the importance of a book such as this one for pediatric patient care, turning our initial ideas into a reality, and providing their superb administrative and editorial assistance from beginning to end.

It is understandable that writing a book such as this can be often challenging because it is trying to catch a moving target in the field of rapid technical advancement in MR imaging. However, our overarching hope is that the contents of this book will increase interest and understanding of pediatric body MR imaging that can enhance the care of pediatric patients with various congenital and acquired disorders. Then, we will have accomplished our overarching goal that we have set with this edition. We truly look forward to feedback from readers that can be incorporated into the next edition. Until then, we sincerely hope that all readers enjoy this book and learn as much as we did in preparing and writing it.

Boston, MA, USA Edward Y. Lee, MD, MPH

Contents

Editors and Contributors

Editor

Edward Y. Lee, MD, MPH Division of Thoracic Imaging, Department of Radiology, Boston Children's Hospital, Harvard Medical School, Boston, MA, USA

Associate Editors

Mark C. Liszewski, MD Division of Pediatric Radiology, Departments of Radiology and Pediatrics, The Children's Hospital at Montefiore and Montefiore Medical Center, Bronx, NY, USA

Michael S. Gee, MD, PhD Division of Pediatric Imaging, Department of Radiology, Massachusetts General Hospital, Harvard Medical School, Boston, MA, USA

Ricardo Restrepo, MD Department of Interventional Radiology and Body Imaging, Nicklaus Children's Hospital, Miami, FL, USA

Pedro Daltro, MD, PhD Alta Excelência Diagnóstica and Department of Radiology, Clínica Diagnóstico por Imagem (CDPI), Rio de Janeiro, Brazil

Assistant Imaging Editor

Heron Werner Junior, MD, PhD Alta Excelência Diagnóstica and Department of Radiology, Clínica Diagnóstico por Imagem (CDPI), Rio de Janeiro, Brazil

Contributors

Sudha A. Anupindi, MD Department of Radiology, The Children's Hospital of Philadelphia, Perelman School of Medicine, University of Pennsylvania, Philadelphia, PA, USA

Susan J. Back, MD Department of Radiology, The Children's Hospital of Philadelphia, University of Pennsylvania, Philadelphia, PA, USA

Gerald Behr, MD Department of Radiology, Memorial Sloan Kettering Cancer Center, New York, NY, USA

James M. Brian, MD Department of Radiology, Penn State Hershey Children's Hospital, Penn State College of Medicine, Hershey, PA, USA

Juan S. Calle Toro, MD Department of Radiology, The Children's Hospital of Philadelphia, University of Pennsylvania, Philadelphia, PA, USA

Pierluigi Ciet, MD, PhD Department of Radiology and Nuclear Medicine; Department of Pediatric Pulmonology, Sophia Children's Hospital Erasmus Medical Center, Rotterdam, The Netherlands

Monica Epelman, MD Department of Radiology, Nemours Children's Health System, Nemours Children's Hospital, University of Central Florida College of Medicine, Orlando, FL, USA

Michael S. Gee, MD, PhD Division of Pediatric Imaging, Department of Radiology, Massachusetts General Hospital, Harvard Medical School, Boston, MA, USA

Sharon W. Gould, MD Department of Medical Imaging, Nemours Children's Health System, A. I. DuPont Hospital for Children, Wilmington, DE, USA

Mary-Louise C. Greer, MBBS, FRANZCR Department of Diagnostic Imaging, The Hospital for Sick Children, University of Toronto, Toronto, ON, Canada

Samantha G. Harrington, MD, MSc Department of Radiology, Massachusetts General Hospital, Boston, MA, USA

Alison R. Hart, MD Diagnostic Imaging, Rhode Island Hospital, Brown University, Providence, RI, USA

Nathan C. Hull, MD Department of Radiology, Mayo Clinic, Rochester, MN, USA

Monica Johnson, MD, MPH Department of Radiology, Massachusetts General Hospital, Harvard Medical School, Boston, MA, USA

Kyung Rae Kim, MD Division of Interventional Radiology, Department of Radiology, UNC Medical Center/University of North Carolina School of Medicine, Chapel Hill, NC, USA

Benjamin M. Kozak, MD Department of Radiology, Massachusetts General Hospital, Harvard Medical School, Boston, MA, USA

Rekha Krishnasarma, MD Department of Radiology, Boston Children's Hospital, Harvard Medical School, Boston, MA, USA

Jessica Kurian, MD Department of Radiology, Montefiore Medical Center, Albert Einstein College of Medicine, Bronx, NY, USA

Edward Y. Lee, MD, MPH Division of Thoracic Imaging, Department of Radiology, Boston Children's Hospital, Harvard Medical School, Boston, MA, USA

Teresa Liang, MD Department of Radiology, Boston Children's Hospital, Harvard Medical School, Boston, MA, USA

Department of Radiology, University of Alberta/Stollery Children's Hospital, Edmonton, AB, Canada

Mark C. Liszewski, MD Division of Pediatric Radiology, Departments of Radiology and Pediatrics, The Children's Hospital at Montefiore and Montefiore Medical Center, Bronx, NY, USA

Archana Malik, MD Department of Radiology, St. Christopher's Hospital for Children, Drexel University College of Medicine, Philadelphia, PA, USA

Amirkasra Mojtahed, MD Division of Pediatric Imaging, Department of Radiology, Massachusetts General Hospital, Harvard Medical School, Boston, MA, USA

Michael M. Moore, MD Department of Radiology, Penn State Hershey Children's Hospital, Penn State College of Medicine, Hershey, PA, USA

Katherine Nimkin, MD Division of Pediatric Imaging, Department of Radiology, Massachusetts General Hospital, Harvard Medical School, Boston, MA, USA

Harriet J. Paltiel, MD Department of Radiology, Boston Children's Hospital, Harvard Medical School, Boston, MA, USA

Daniel J. Podberesky, MD Department of Radiology, Nemours Children's Health System, Nemours Children's Hospital, University of Central Florida College of Medicine, Orlando, FL, USA

Anil G. Rao, MBBS, DMRD, DNB Desert Radiology, Las Vegas, NV, USA

Ricardo Restrepo, MD Department of Interventional Radiology and Body Imaging, Nicklaus Children's Hospital, Miami, FL, USA

Gary R. Schooler, MD Department of Radiology, Duke University Medical Center, Durham, NC, USA

Abdusamea Shabani, MB BCh FRCR Division of Body and Diagnostic Imaging, Sidra Medicine, Doha, Qatar

Raja Shaikh, MD Division of Interventional Radiology, Department of Radiology, Boston Children's Hospital, Harvard Medical School, Boston, MA, USA

Jennifer K. Son, MD Division of Pediatric Radiology, Russell H. Morgan Department of Radiology and Radiological Sciences, Johns Hopkins University School of Medicine, Baltimore, MD, USA

Jeffrey J. Tutman, MD Division of Pediatric Radiology, Department of Radiology, Children's Hospital of Colorado, University of Colorado School of Medicine, Aurora, CO, USA

Lung and Pleura

1

Mark C. Liszewski, Pierluigi Ciet, and Edward Y. Lee

Introduction

Disorders of the lungs and pleura are common in children and are a frequent indication for medical imaging. Over the past decade, a combination of advances in magnetic resonance (MR) imaging scanner technology and increased concern about the effects of ionizing radiation has led to increased utilization of MR imaging in the pediatric population. Despite this general trend, there has been slower adoption of MR imaging to evaluate the lungs and pleura due to technical limitations including motion artifact, low signal-to-noise ratios, and signal dephasing at air-tissue interfaces. As MR imaging technology advances, many of these technical hurdles are being overcome, and MR imaging of the lungs and pleura has begun to be a feasible option for evaluation of many pediatric pleuropulmonary conditions. Therefore, an up-to-date understanding of these emerging applications is important to practitioners performing MR imaging in infants and children.

In this chapter, an overview of MR imaging techniques to evaluate the lungs and pleura in children is discussed. Normal anatomy and development of the lungs and pleura are described, and the MR imaging findings in a spectrum of pediatric lung and pleural disease are illustrated.

M. C. Liszewski (✉)
Division of Pediatric Radiology, Departments of Radiology and Pediatrics, The Children's Hospital at Montefiore and Montefiore Medical Center, Bronx, NY, USA

P. Ciet
Department of Radiology and Nuclear Medicine, Department of Pediatric Pulmonology, Sophia Children's Hospital Erasmus Medical Center, Rotterdam, The Netherlands

E. Y. Lee
Division of Thoracic Imaging, Department of Radiology, Boston Children's Hospital, Harvard Medical School, Boston, MA, USA

Magnetic Resonance Imaging Techniques

A main advantage of MR imaging is the ability to obtain cross-sectional images with high-contrast resolution without requiring ionizing radiation. Because of technical challenges when imaging the lungs and pleura, the key to successful MR imaging of the thorax lies in appropriate patient preparation and use of optimized pulse sequences and protocols.

Patient Preparation

MR imaging is an imaging modality that is highly sensitive to motion artifact, and successful MR imaging of the chest depends on appropriate patient selection and preparation prior to imaging. Selection of a successful technique largely depends on the age of the child and the assessment of the child's ability to follow instructions.

Infants are often able to undergo successful MR imaging utilizing a "feed and wrap" technique, in which the child is fed and swaddled prior to MR imaging [1]. After infancy, nearly all children under 5 years of age are not able to hold still or adequately follow breathing instructions and therefore require moderate sedation or general anesthesia for successful MR imaging. Examinations performed under moderate sedation must utilize sequences that are optimized for quite free breathing. Examinations performed under general anesthesia may utilize sequences that require apnea. Children as young as 5 years of age may be candidates for MR imaging without sedation or anesthesia but must be carefully assessed prior to imaging to gauge their ability to cooperate for the examination. In order for an examination to be successful, preparation and coaching are essential prior to the MR imaging. Children must practice breathing maneuvers and become familiar with the scanner prior to the examination, ideally in a mock scanner environment with the assistance of child life specialists. During practice sessions, children learn to hold their breaths at end-inspiration and end-expiration, rapidly breathe in and out, and perform coughing maneuvers.

E. Y. Lee et al. (eds.), *Pediatric Body MRI*, https://doi.org/10.1007/978-3-030-31989-2_1

MR Imaging Pulse Sequences and Protocols

Historically, MR imaging of the lungs and pleura has been hampered by technical factors inherent to these organ systems including respiratory motion artifact, low signal-to-noise ratios, and signal dephasing at air-tissue interphases. However, in recent years, technological advances have helped to overcome many of these impediments, and diagnostic MR imaging of the lungs and pleura can now be achieved on MR imaging scanners currently in use at many medical centers. MR imaging protocols of the lungs and pleura mainly consist of spin-echo and gradient-echo sequences which can often produce image quality that approaches that of CT [2]. Newer techniques including ultra-short (UTE) or zero echo time (ZTE) sequences provide even better image quality which is on par with CT [3, 4]. When pediatric patients are unable to cooperate with breathing instructions, respiratory gating can be employed by utilizing a pneumobelt or navigator echo sequence [2]. Specialized sequences, which minimize motion artifact, can be used to obtain images during free breathing, including helicoidal (PROPELLER@GE) or radial (STARVIBE@SIEMENS) k-space acquisition schemes [5, 6]. MR imaging also has the ability to provide information about ventilation, inflammation, perfusion, and structure, under the acronym VIPS [7–10].

Table 1.1 MR imaging sequences for ventilation, inflammation, perfusion, and structural (VIPS) MR imaging of the lung and pleura

SEQUENCE	ACRONYMS	MR IMAGING SYSTEM	AVERAGE ACQUISITION TIME (FOR THE ENTIRE CHEST COVERAGE)	SPATIAL RESOLUTION	TEMPORAL RESOLUTION	SCAN PARAMETERS
Ventilation						
2D gradient echo	SSFP (GE) TruFISP (SIEMENS) bFFE (PHILIPS)	1.5 T	3–9 min	FOV = 450 × 450 mm SL = 12 mm Matrix = 128 × 128	3.33 images/s acquisition	TE/TR 0.67 ms/1.46 ms FA = 65° BW = 2056 Hz/pixel
2D gradient echo	2D SPGR (GE) 2D FLASH (SIEMENS) 2D FFE	1.5 and 3 T	3–9 min	FOV = 500 × 500 mm SL = 15 mm Matrix = 256 × 192	3.08 images/s acquisition	TE/TR 1.04 ms/3 ms FA = 5° BW = 1500 Hz/pixel
Inflammation						
2D single-shot echo- planar imaging sequence (EPI)	EPI-DWI (SIEMENS/GE/ PHILIPS)	1.5 T	5–7 min	FOV SL = 5 mm Matrix	Low	TE/TR 83 ms/5632 ms FA = 90° B = 0 and 600 s/mm^2
2D single-shot echo- planar imaging sequence (EPI)	EPI-DWI	1.5 T	5–7 min	Voxel size 2.5 × 2.5 × 6 mm^3	Low	TE/TR 54 ms/4800 ms FA = 90° BW = 1644 Hz/pixel B = 0, 10, 20, 30, 50, 70, 100, 150, 200, 400, 800 s/mm^2
2D T2-weighted Turbo spin echo	TSE (SIEMENS) FSE (GE) TSE (PHILIPS)	1.5 T and 3 T	5–7 min	FOV = 400 mm SL = 5–7 mm Matrix = 256 × 192	Low	TE/TR 80 ms/2000–4000 ms FA = 90° BW = 1644 Hz/pixel Fat suppression mode = SPAIR
Perfusion/Angiography						
2D gradient echo	SSFP (GE) TruFISP (SIEMENS) bFFE (PHILIPS)	See scan parameters above				
2D gradient echo	2D SPGR (GE) 2D FLASH (SIEMENS) 2D FFE	See scan parameters above				
3D gradient echo T1-weighted	FLASH 3D (SIEMENS) SPGR (GE) FFE (PHILIPS)	1.5 and 3 T	12–20 s	FOV = 460 mm matrix = 40 × 192 × 256 (isotropic voxel as low as 1 mm^3)	Low	TR = 2.5–3 ms TE = 1.0–1.5 ms FA = 30°–40°
3D gradient echo T1-weighted	Twist(SIEMENS) TRICKS (GE) TRACK (PHILIPS)	1.5 and 3 T	Breath-hold (end-expiratory)/ shallow breathing	FOV = 460 mm matrix = 32 × 96 × 128	High, 0.5–1 s/ volume	TR = 2.0–2.5 ms TE = 0.8–1.0 ms FA = 30°–40°

Table 1.1 (continued)

SEQUENCE	ACRONYMS	MR IMAGING SYSTEM	AVERAGE ACQUISITION TIME (FOR THE ENTIRE CHEST COVERAGE)	SPATIAL RESOLUTION	TEMPORAL RESOLUTION	SCAN PARAMETERS
Structure						
2D	T2-weighted BLADE (SIEMENS) T2-weighted PROPELLER (GE) T2-weighted MultiVane (PHILIPS) ± FAT suppression	1.5 and 3 T	End-expiratory with navigator echo triggering 3 to 7 min according respiratory pace and pattern	FOV: 380–400 mm Matrix = 200 × 200 SL = 5–6 mm, axial and coronal	Low	TR = 1000–2000 TE = 27–60 ms FA = 90°–150°
2D	TRUFISP (SIEMENS) SSFP (GE) Balanced FFE (PHILIPS)	1.5 T	12–20 s	FOV = 400 mm Matrix = 160 × 160 SL 2.5–5 mm	High	TR = 1.08 ms TE = 0.42 ms FA = 20° BW = 1776 Hz/pixel
3D	SPACE (SIEMENS) CUBE (GE) VISTA (PHILIPS)	1.5 T–3 T	End-expiratory with navigator echo triggering 5 min	FOV = 320 mm Matrix = 160 × 160 SL = 2 mm	Low	TR = 940 ms TE = 60 ms FA = 90° BW = 355 Hz/pixel Echo train length = 120
3D	VIBE(SIEMENS) SPGR (GE) THRIVE (PHILIPS)	1.5 T–3 T	Breath-hold 10–12 s (inspiratory and expiratory)	FOV = 400 mm Matrix = 200 × 200 SL = 2 mm	High	TR = 1.7 ms TE = 0.7 ms FA = 2° BW = 862 Hz/pixel
3D	STARVIBE (SIEMENS) Not available for GE and PHILIPS	1.5 T–3 T	Free-breathing 3–5 min	FOV = 400 mm Matrix = 320 × 320 SL = 4 mm	Low	TR = 7.46 ms TE = 2.46 ms FA = 9° BW = 820 Hz/pixel
3D	LAVA FLEX (GE)	1.5 T–3 T	Breath-hold (10 s)	FOV = 260 mm Matrix = 128 × 128 SL = 3 mm	High	TR = 3.7 ms TE = min full ms FA = 1°
3D	PETRA(SIEMENS) ZTE(GE) MULTIVANE-XD (PHILIPS)	1.5 T–3 T	Free-breathing 7–10 min	FOV = 360 mm^3 Matrix size = 416 mm^3	Low	TR = 4.1 ms TE = 0.07 ms

Adapted from Liszewski et al. [11], with permission
GE General Electric, Boston, Massachusetts, USA, *Siemens* Munich, Germany, *Philips* Amsterdam, Netherlands

Table 1.1 provides an outline of MR imaging sequences commonly used to image the lungs and pleura [11].

Anatomy

Embryology

Lung Development The development of the lung begins in the first gestational month and continues after birth into childhood. The development is divided into five phases: embryonic, pseudoglandular, canalicular, saccular, and alveolar.

Phases of Prenatal Lung Development During the fourth week of gestation, lung development begins when the laryngotracheal groove arises from the foregut endoderm and forms the lung bud. The embryonic phase begins when the lung bud divides into the right and left bronchial buds [12]. In the embryonic phase, the bronchial buds lengthen and divide into three branches on the right and two branches on the left and further subdivide into the pulmonary segments. By the end of the embryonic phase, a vascular plexus begins to form within the lung mesenchyme [13] (Fig. 1.1).

The pseudoglandular phase begins at week 5 and ends at week 17. In this phase, the bronchi further divide, and by week 17, the entire air-conducting portion of the lung has developed to the level of the terminal bronchiole. On the cellular level, ciliated, goblet, and neuroendocrine cells develop, and the terminal bronchioles contain cuboid columnar cells (see Fig. 1.1).

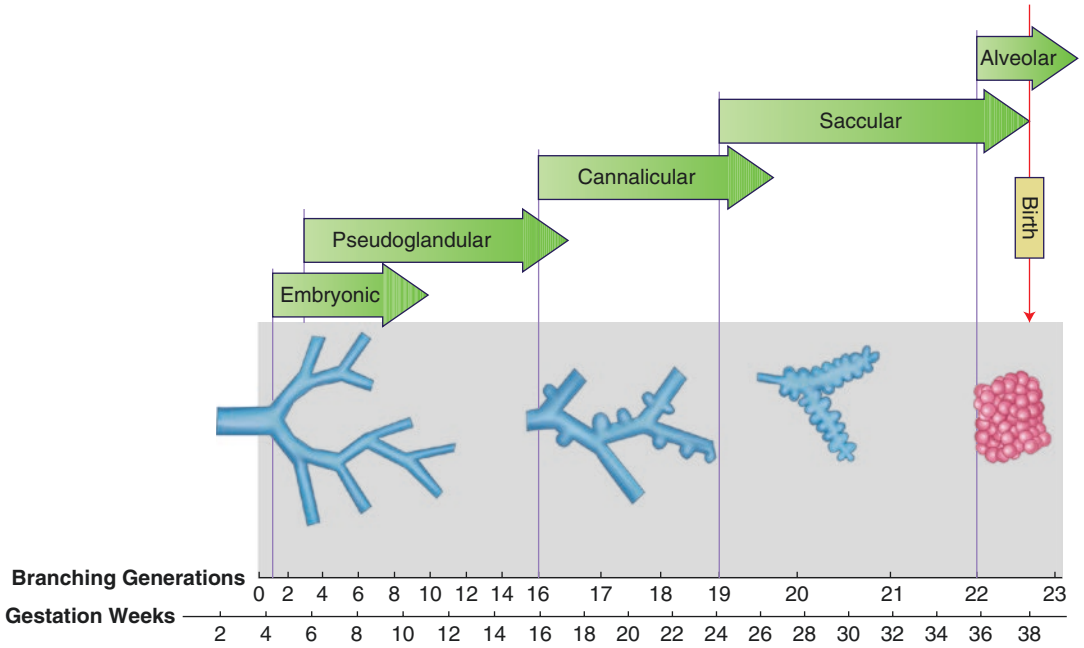

Fig. 1.1 Diagram showing prenatal lung development

The canalicular phase begins at week 17 and ends at week 28. The portion of the lung involved in oxygen exchange develops during this phase, including the respiratory bronchioles, alveolar ducts, and alveoli. Type I pneumocytes begin to develop in this phase, and Type II pneumocytes contain surfactant proteins but do not secrete them. The alveolar capillary bed begins to form at this stage. By the end of the canalicular phase, gas exchange is possible, and survival outside the uterus is feasible, but only with intensive medical care, exogenous surfactant therapy, and mechanical ventilation (see Fig. 1.1).

The saccular phase begins at week 29 and ends at week 36. Alveolar sacculi proliferate during this phase, and the basal lamina of the distal respiratory epithelium fuses with the basal lamina of the alveolar capillary endothelium, allowing for improved gas exchange. Surfactant begins to be excreted during this phase, but its production is not yet at the levels of a full-term newborn, and children born at this phase usually require exogenous surfactant therapy [14] (see Fig. 1.1).

The alveolar phase begins at week 36 and continues through 18 months of age. Throughout this phase, more alveoli form, leading to approximately 50 million alveoli soon after birth and 300 million alveoli by the time the lung is fully mature. With alveolar development, the pulmonary alveolar capillary network also grows, leading to increased capacity for gas exchange [15] (see Fig. 1.1).

Fetal Lung Fluid and Surfactant Fetal lung fluid fills the airways and alveoli while in utero. Although it mixes with amniotic fluid, the composition of fetal lung fluid is different than that of amniotic fluid. Fetal lung fluid is produced by the respiratory epithelium. At term, approximately 5 mL/kg/hour. of lung fluid is produced [16]. During labor and immediately after birth, fetal lung fluid is cleared by pulmonary lymphatics [17].

Surfactant is composed of phospholipids, protein, neutral lipids, and cholesterol and is found within fetal lung liquid in the later stages of gestation. Intracellular surfactant is present within Type II pneumocytes in the canalicular phase at 20–24 weeks gestation and can be found within fetal lung fluid starting in the saccular phase [17]. Surfactant produced before 35 weeks gestation is present in smaller amounts and is more susceptible to inactivation than after 35 weeks [17, 18]. Surfactant allows alveoli to expand during inspiration by reducing surface tension [19, 20]. Surfactant is essential to lung function, and a major complication of pre-term birth is surfactant deficiency disorder (SDD). When a pre-term birth is imminent, pregnant mothers can be treated with glucocorticoids to speed up endogenous surfactant production by the fetus. After birth, exogenous surfactant may be administered via endotracheal tube to treat SDD.

Pleural Development The pleura begins development before the lungs at 3 weeks gestation. At this time, the pleura begins to form from the mesoderm along with the pericardium and peritoneum [21]. At 9 weeks gestation, the pleura separates from the pericardium and peritoneum. The pleura is comprised of the visceral pleural, which covers the lung, and the parietal pleura, which covers the chest wall and diaphragm [21] (Fig. 1.2).

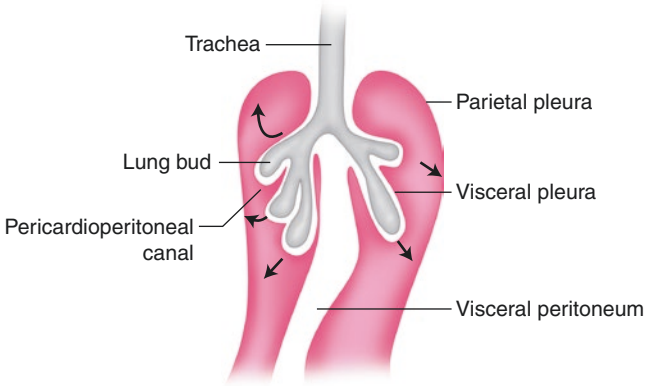

Fig. 1.2 Diagram showing pleural development

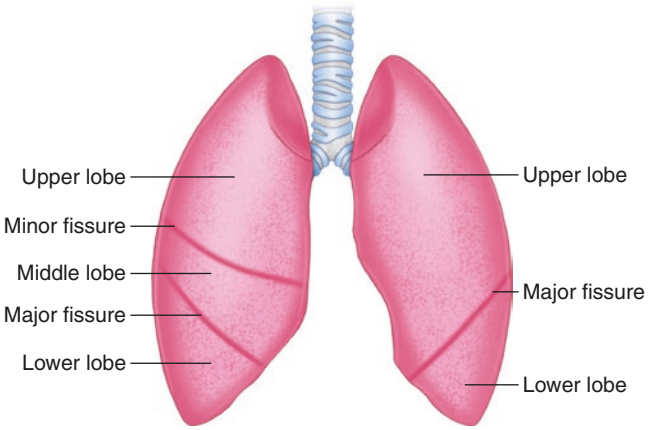

Fig. 1.3 Diagram of lobar anatomy: sections of normal lung

Normal Development and Anatomy

Lobar Anatomy The right lung is composed of three lobes (upper, middle, and lower), and the left lung is composed of two lobes (upper, which includes the lingua, and lower) (Fig. 1.3). Each lobe is separated by a pleura-lined fissure. Each lobe is further divided into segments, which are defined by segmental bronchi and not divided by fissures. Table 1.2 describes the segments in each lobe.

Lung Parenchyma

Secondary Pulmonary Lobule The secondary pulmonary lobule is the smallest structural unit of the lung that may be visible on MR imaging; smaller structures such as the pulmonary acini and alveoli are too small to be visualized as discrete structures. Each secondary pulmonary lobule has a polyhedral shape and is bordered by connective tissue septations called interlobular septa (Fig. 1.4). At birth, secondary pulmonary lobules have a mean diameter of 3 mm and are therefore not visible on most conventional MR imaging sequences. However, they are visible in older children and adults on MR imaging, and they reach a diameter of 13–20 mm in adulthood

Table 1.2 Lung lobes and segments

Lobes	Segments
Right upper	Apical, posterior, and anterior
Right middle	Lateral and medial
Right lower	Superior, medial basal, anterior basal, lateral basal, and posterior basal
Left upper	Apicoposterior, anterior, superior lingular, and inferior lingular
Left lower	Superior, medial basal, anterior basal, lateral basal, and posterior basal

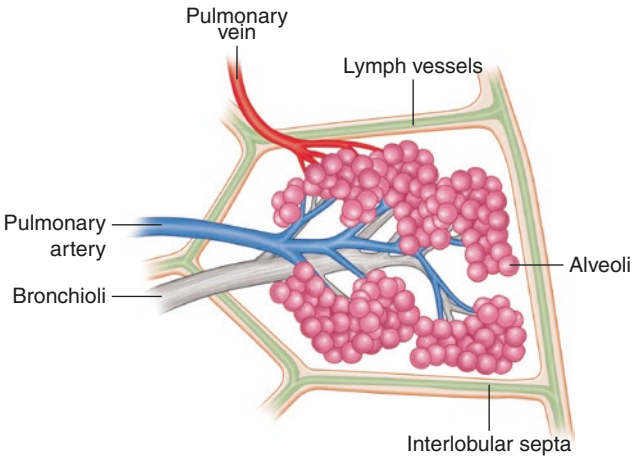

Fig. 1.4 Diagram of lung parenchyma: secondary pulmonary lobule

[22]. A lobular bronchiole is in the center of each secondary pulmonary lobule and communicates with up to 25 terminal bronchioles and their acini [23, 24].

Acini and Alveoli Acini and alveoli are the functional units of the lung where gas exchange occurs. These structures are too small to be visualized as discrete structures on MR imaging. Each lobular bronchiole communicates with up to 25 terminal bronchioles, which communicate with acini and alveoli [23, 24] (Fig. 1.5). When filled with air, groups of acini and alveoli appear uniformly hypointense, and when filled with fluid or other material, they appear uniformly intense because the alveolar walls are beyond the spatial resolution of MR imaging.

Vascular Anatomy Deoxygenated blood moves through the lungs to the alveolar capillaries via the pulmonary arteries, which travel along with bronchi and bronchioles in bronchovascular bundles. The smallest pulmonary arterial branch that can be visualized on MR imaging is the lobular artery which travels in the center of the secondary pulmonary lobule along with the lobular bronchiole. Lobular arteries branch into intralobular and acinar arteries which are beyond the spatial resolution of MR imaging. These small pulmonary artery branches supply an extensive alveolar capillary bed, where gas exchange occurs. Oxygenated blood then enters pulmonary venules,

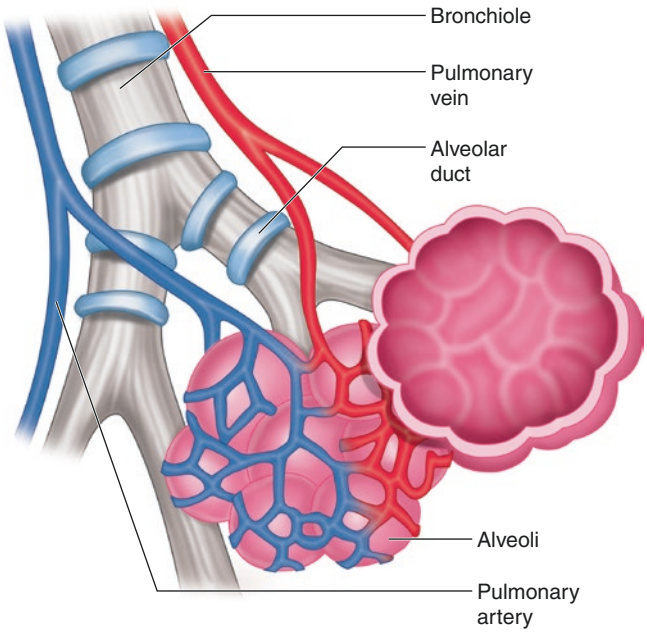

Fig. 1.5 Diagram of acini and alveoli: structure of the lung

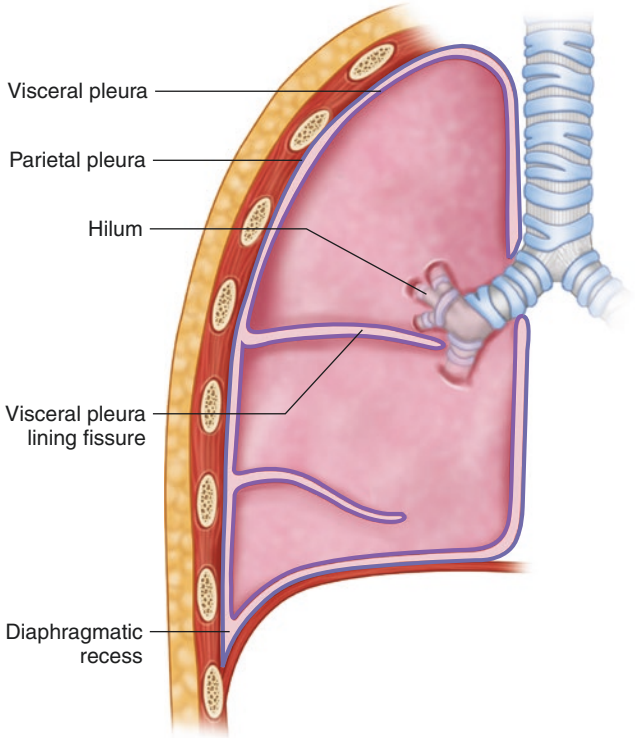

Fig. 1.6 Diagram of pleural anatomy: parietal and visceral pleura

which are located within the interlobular septa, separate from the bronchovascular bundles. Pulmonary arteries and veins therefore travel separately, except in the hila where they are adjacent to one another.

A small amount of oxygenated blood is supplied to the lung via bronchial arteries to provide oxygen to the metabolically active tissues in the trachea, bronchi, and pulmonary arteries [9]. Venous drainage of these structures is primarily via systemic bronchial veins, which continue to the right side of the heart via hemiazygous and azygous veins.

Lymphatic Anatomy Pulmonary lymphatics are comprised of a deep plexus and superficial plexus [25]. The deep plexus is located within the bronchovascular bundles in the center of the secondary pulmonary lobule. The superficial plexus travels alongside pulmonary venules within the interlobular septa [23, 25].

Pleural Anatomy

Parietal and Visceral Pleura The pleural space is formed by two pleural membranes: the parietal pleura and the visceral pleura (Fig. 1.6). Each is comprised of a single layer of mesothelial cells, a basement membrane, and a layer of connective tissue which contains blood vessels and lymphatics [21]. The arterial supply to the parietal pleura is via the intercostal arteries, and the visceral pleura is supplied by bronchial arteries. Normal pleural fluid is produced from systemic pleural arteries in both the visceral and parietal pleura [21].

The visceral and parietal pleura both have extensive lymphatic channels. Fluid within the pleural space drains via parietal pleural lymphatics, but not visceral pleural lymphatics [21].

Pleural Fissures The visceral pleura is tightly adherent to the surface of the lung parenchyma and forms the pleural fissures where it invaginates between lobes of the lung (see Fig. 1.6). The right lung contains a major fissure which separates the right lower lobe from the right upper and middle lobes and a minor fissure, which separates the right upper lobe and the right middle lobe. The left lung contains only a major fissure, which separates the left upper lobe and left lower lobe.

Anatomic Variants

Accessory Pleural Fissures and Lobes Accessory pleural fissures and lobes are relatively common normal variants, seen in approximately 30% of the population [26, 27]. Accessory fissures include (in order of frequency) inferior accessory fissure (12–21%), left minor fissure (8–9%), superior accessory fissure (1–5%), fissure between the medial and lateral segments of the right middle lobe (2–5%), fissure between the superior and inferior segments

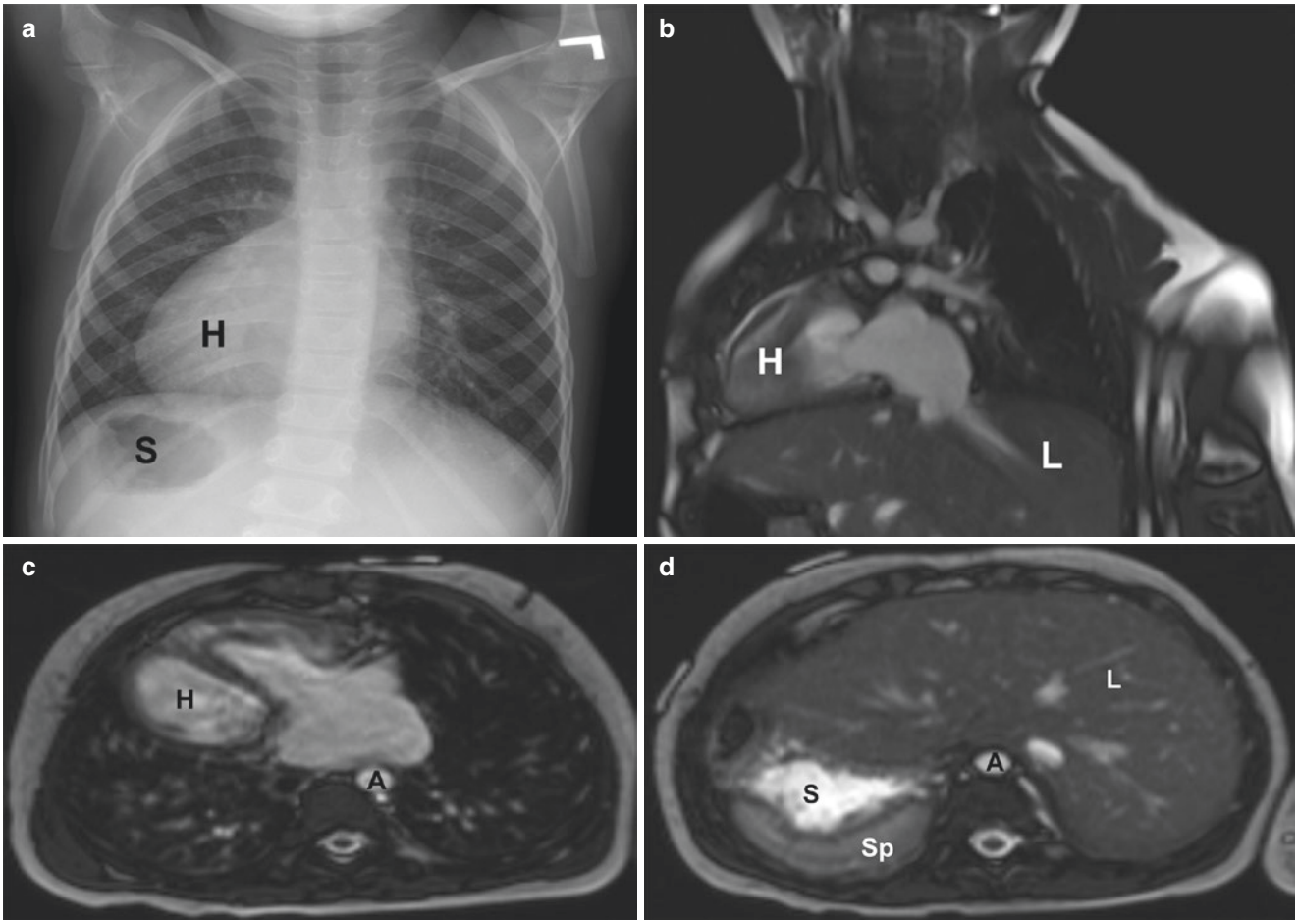

Fig. 1.7 Heterotaxy syndrome in a 4-year-old girl. (**a**) Frontal chest radiograph shows a right-sided heart (H) and stomach (S). (**b**) Coronal oblique non-enhanced bright-blood MR image shows right-sided heart (H) and left-sided liver (L). (**c**) Axial non-enhanced bright-blood MR image shows right-sided heart (H) and left-sided descending thoracic aorta (A). (**d**) Axial non-enhanced bright-blood MR image shows left-sided liver (L), right-sided stomach (S), right-sided spleen (Sp), and midline abdominal aorta (A)

of the lingula (1–5%), and fissure between the anterobasal and laterobasal lower lobe segments (2.5–3%) [26, 27].

The azygous fissure is another type of accessory fissure, but it has a different origin than the other accessory fissures. An azygous fissure forms when the azygous vein takes an anomalous lateral course during development and bisects the right upper lobe. Therefore, the azygous fissure is lined by parietal and visceral pleura, unlike the other fissures, which are composed of only visceral pleura.

Heterotaxy Syndromes Heterotaxy syndromes are a group of conditions in which the location and laterality of structures is altered (Fig. 1.7). The simplest example is situs inversus totalis, where all structures are flipped from left to right. In the lungs, situs inversus totalis manifests as a three-lobed left lung and two-lobed right lung. More complex heterotaxy syndromes may occur in which both lungs have three lobes (right isomerism) or both lungs have two lobes (left isomerism). Right isomerism is associated with asplenia and left isomerism is associated with polysplenia.

Spectrum of Lung and Pleural Disorders

In the following sections, the MR imaging findings in a spectrum of congenital and acquired lung and pleural disorders affecting children are presented. Pertinent clinical features and current treatments are also discussed.

Congenital and Developmental Lung Disorders

Bronchial Atresia Bronchial atresia is a congenital thoracic lesion characterized by developmental interruption,

or atresia, of a bronchus. There are two main theories about the underlying etiology of bronchial atresia. The first proposes that an ischemic event after bronchial development leads to obliteration of the bronchus. The second proposes a primary disruption of proximal bronchial bud development affecting only the proximal portion of the bronchus but not affecting the distal portion. In either case, the lung distal to the atretic bronchus does not communicate with the central airway. Pulmonary secretions are unable to pass through the atretic bronchus, and the bronchus distal to the atresia eventually fills with fluid, forming a bronchocele. The lung distal to the atretic bronchus becomes hyperinflated due to a check-valve mechanism or air drift via collateral pathways of aeration [28]. The air within the hyperinflated lung becomes deoxygenated, and the vascularity decreases due to hypoxia-induced vasoconstriction.

Bronchial atresia may be detected on prenatal ultrasound, and prenatal MR imaging may be utilized to characterize the lesion. In utero, amniotic fluid rather than air becomes trapped within the lung distal to the atretic bronchus, and prenatal MR imaging characteristically demonstrates hyperintense hyperexpanded region of the lung on T2-weighted imaging due to trapped fluid [28]. If not detected on prenatal imaging, bronchial atresia may be first detected on chest radiographs. Chest radiograph demonstrates a round or oval perihilar opacity representing the bronchocele often with adjacent lucent overinflated segment of the lung.

Whether detected in utero or on chest radiograph, postnatal cross-sectional imaging is often obtained to further evaluate and confirm bronchial atresia, especially when surgical resection is being considered. In current practice, this is most often achieved with contrast-enhanced CT; however, MR imaging has also been described for this indication. MR imaging depicts the bronchocele as a tubular perihilar structure which is hyperintense on T1- and T2-weighted images and does not enhance on post contrast images [29, 30]. Hyperinflation within the distal lung is not as easily depicted on MR imaging as on CT due to the proton-poor environment within the air-filled hyperexpanded lung [31].

When symptomatic, bronchial atresia is treated with surgical resection. Management of small asymptomatic bronchial atresia is currently controversial, with some recommending resection due to risk of superinfection and others favoring a conservative approach [32, 33].

Congenital Lobar Emphysema Congenital lobar emphysema (CLE) or also known as congenital lobar overinflation is characterized by hyperexpansion of a lobe of the lung due to narrowing of a lobar bronchus. CLE occurs in certain lobes more frequently, occurring in the left upper lobe > right middle lobe > right upper lobe > right or left lower lobe [34]. It can also affect more than one lobe. CLE often produces symptoms soon after birth due to progressive lobar hyperexpansion, and treatment consists of lobectomy.

CLE may be detected on prenatal ultrasound, and prenatal MR imaging may be utilized to characterize the lesion. In utero, amniotic fluid rather than air becomes trapped within the hyperexpanded lobe, and prenatal MR imaging characteristically demonstrates hyperintense hyperexpanded lobe of lung on T2-weighted imaging due to trapped fluid. CLE and bronchial atresia have similar findings on fetal MR imaging, and differentiating between the two is often difficult. If not detected on prenatal imaging, CLE may be detected on chest radiographs in the newborn period demonstrating progressive hyperexpansion of a lobe of the lung.

Whether detected in utero or on chest radiograph, postnatal cross-sectional imaging is often obtained to further evaluate, characterize, and confirm CLE, especially when surgical resection is being considered. In current practice, this is most often achieved with CT. MR imaging has a limited role for this indication, because the proton-poor hyperexpanded lung is not as well characterized on MR imaging. With newer imaging techniques that improve MR imaging resolution (such as UTE and ZTE sequences), MR imaging may play a larger role in the future. On MR imaging, CLE appears as a hypointense hyperexpanded lobe of the lung, often with accompanying mediastinal shift and ground-glass signal abnormality within the adjacent lobes due to compressive atelectasis.

Currently, asymptomatic children or those with only mild symptoms are often managed conservatively with continuous follow-up to assess possible interval resolution or stability, whereas lobectomy by open or thoracoscopic approach is employed for symptomatic pediatric patients.

Bronchogenic and Other Foregut Duplication Cysts Bronchogenic cysts are a type of foregut duplication cyst that occurs due to abnormal budding of the ventral lung bud or abnormal branching of the tracheobronchial tree during lung development. Most bronchogenic cysts develop in close proximity to the central tracheobronchial tree, and most are located within the mediastinum, but approximately 15% are located within the lung parenchyma (Fig. 1.8) [35]. Esophageal duplication cysts and neurenteric cysts are other types of foregut duplication cysts, which are related to

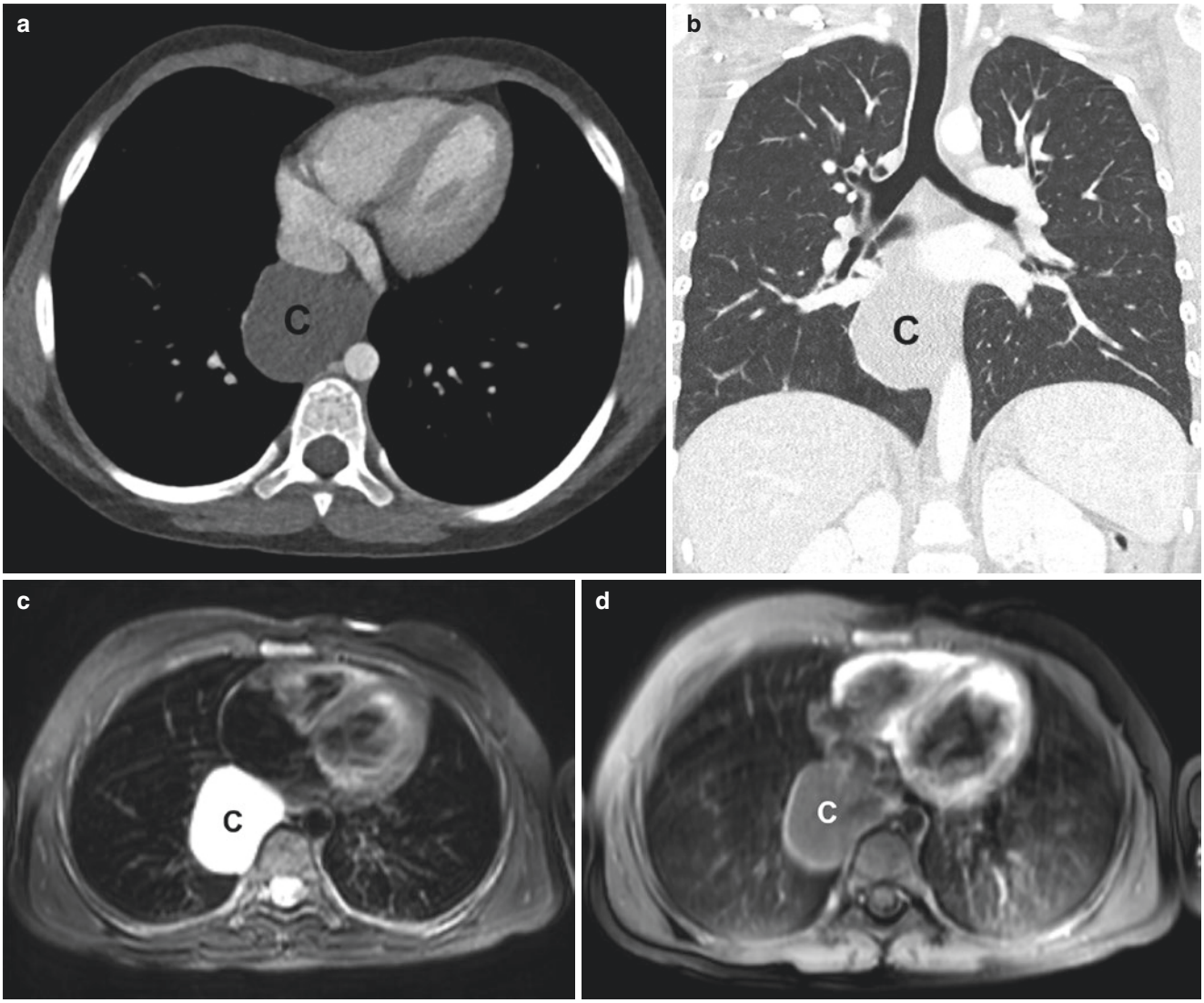

Fig. 1.8 Bronchogenic cyst in a 7-year-old girl. (**a**) Axial enhanced soft tissue window setting CT image shows a thin-walled cyst (C) in the right posterior mediastinum containing simple fluid density. (**b**) Coronal enhanced lung window setting CT image shows the thin-walled cyst (C). (**c**) Axial non-enhanced bright-blood short tau inversion recovery (STIR) MR image shows hyperintense signal within the cyst (C). (**d**) Axial enhanced T1-weighted fat-suppressed MR image shows the cyst (C) with a thin enhancing wall and no central enhancement

bronchogenic cysts (Fig. 1.9). Esophageal duplication cysts arise from the dorsal bud of the primitive foregut, and neurenteric cysts occur due to incomplete separation of the endoderm and notochord. Although often treated as distinct lesions, foregut duplication cysts frequently contain elements of more than one foregut tissue, and hybrid lesions are common.

Bronchogenic and other foregut duplication cysts are most often detected as incidental findings in asymptomatic infants and children. They may be diagnosed on prenatal imaging, and fetal MR imaging typically demonstrates a unilocular thin-walled hyperintense cyst within the mediastinum on T2-weighted sequences (Fig. 1.10) [36–38]. If not detected prenatally, bronchogenic and other foregut duplication cysts may be detected on chest radiograph as a mediastinal or pulmonary mass. Cross-sectional imaging is often performed to evaluate the finding of a mass. Although this is most typically achieved with CT, MR imaging is an excellent modality to characterize bronchogenic and other foregut duplication cysts. MR imaging

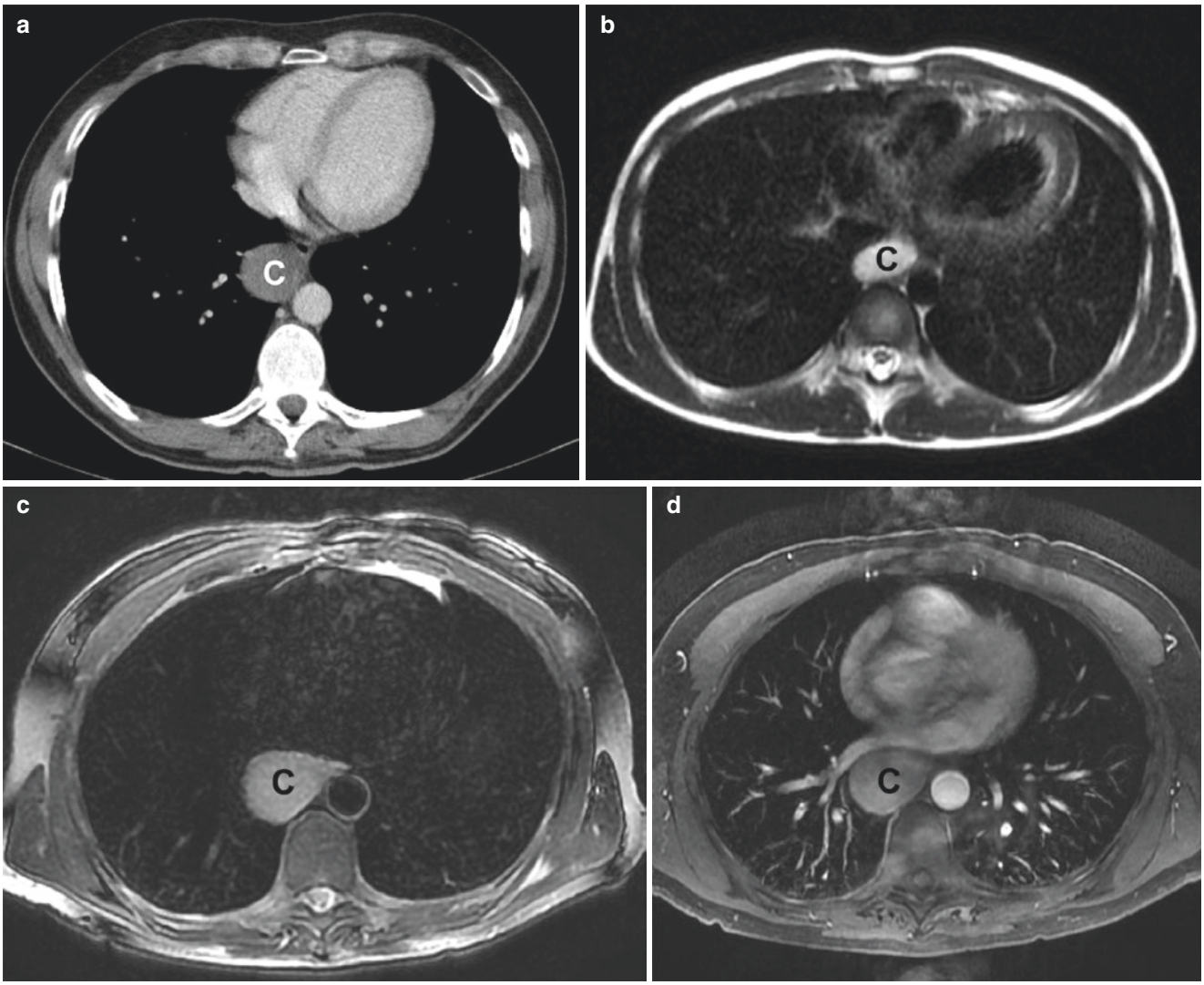

Fig. 1.9 Esophageal duplication cyst in a 12-year-old boy. (**a**) Axial enhanced soft tissue window setting CT image shows a cyst (C) adjacent to the esophagus which is greater than simple fluid density due to proteinaceous contents. (**b**) Axial non-enhanced SSFSE T2-weighted MR image shows hyperintense signal within the cyst (C). (**c**) Axial non-enhanced black-blood T2-weighted MR image shows hyperintense signal within the cyst (C). (**d**) Axial enhanced T1-weighted fat-suppressed MR image shows the cyst (C) with internal hyperintensity due to intrinsically hyperintense proteinaceous material rather than due to enhancement

typically demonstrates a cyst that is hyperintense on T2-weighted images and has variable intensity on T1-weighted images and does not enhance on contrast-enhanced images, except for a thin rim of wall enhancement [34]. Bronchogenic cysts within the mediastinum rarely communicate with the airway, but more peripheral cysts may communicate with the airway and contain an air-fluid level [39]. Bronchogenic cysts may become infected, especially when there is communication with the airway. When superinfected, cysts may develop a thick enhancing wall with irregular borders [40].

Currently, both asymptomatic and symptomatic bronchogenic and other foregut duplication cysts are typically treated with surgical resection [40].

Congenital Pulmonary Airway Malformation Congenital pulmonary airway malformations (CPAMs), previously known as cystic adenomatoid malformations (CCAMs), are a group congenital lung lesions composed of large cysts or microscopic cysts, bronchiolar overgrowth, and abnormal connection with the airway [39, 40]. Classically, CPAMs have conventional pulmonary vascular anatomy,

Fig. 1.10 Bronchogenic cyst on prenatal MR imaging. Coronal non-enhanced T2-weighted image shows a thin-walled cyst (*arrow*) adjacent to the left bronchus

Table 1.3 Congenital pulmonary airway malformation (CPAM) modified Stocker classification

Type	Characteristics
Type 0	Diffuse acinar dysgenesis Incompatible with life and rarely seen in clinical practice
Type 1	Large cyst or cysts measuring >2 cm
Type 2	Cyst or cysts measuring <2 cm
Type 3	Tiny "microcysts" measuring <5 mm Appears as a solid mass on imaging and gross inspection
Type 4	Large cysts in the periphery of the lung Difficult to differentiate from type 1

receiving blood from the pulmonary artery and draining to the pulmonary vein [41]. However, hybrid lesions are common, and elements of CPAM are frequently present in pulmonary lesions supplied by a systemic artery [42–44]. Several classification systems have been developed to describe CPAMs, but the most commonly used system in current practice is the modified Stocker system [39, 40, 42, 44–47]. The modified Stocker system is described in Table 1.3.

CPAMs may be first diagnosed on prenatal imaging. On fetal MR imaging, CPAMs appear as hyperintense lung lesions, and depending on the type discrete cysts may or may not be visible (Fig. 1.11) [48]. Categorization of CPAMs on fetal imaging is slightly different than on postnatal imaging, largely due to the smaller size of the fetus. On fetal imaging, CPAMS are categorized as macrocystic when cysts are ≥5 mm or microcystic when cysts are <5 mm [49]. Macrocystic (≥5 mm) lesions on fetal imaging correspond to Stocker Type 1 lesions, and microcystic (<5 mm) lesions on fetal imaging correspond to Stocker Type 2 lesions [40, 48]. If not detected on prenatal imaging, CPAM may be first visualized on chest radiograph as an air-filled cystic lesion or a solid mass, depending on the type [48].

Postnatal cross-sectional imaging is indicated to further assess CPAM especially when surgical resection is considered. Currently, CT is the modality most often utilized for this indication, but MR imaging can be utilized as an alternative. Because pulmonary sequestration and hybrid lesions are often a differential consideration, MR angiography is indicated to evaluate the vascular supply. MR imaging findings of CPAMs depend on the type. Cysts in type 1, 2, and 4 lesions are air-filled or fluid-filled and have a thin hyperintense wall that enhances on contrast-enhanced images (Fig. 1.12) [31]. Type 3 lesions appear as solid enhancing masses on contrast-enhanced MR images.

If a CPAM is causing symptoms, surgical resection is indicated. Management of asymptomatic CPAM is more variable. Many advocate surgical resection due to small risks of superinfection and associated malignancy, but others recommend a conservative approach due to the small incidence of these complications [50–55].

Pulmonary Sequestration Pulmonary sequestration was defined by Pryce in 1946 as "disconnected bronchopulmonary mass or cyst with an anomalous arterial supply" [56]. Twenty-five percent of lesions are defined as extralobar, with their own pleural covering and venous drainage to a systemic vein [39–41]. Seventy-five percent of lesions are defined as intralobar, sharing a pleural covering with the normal lung and with venous drainage to the left atrium [39–41]. Extralobar sequestration may occur in the lower lobes, within the diaphragm, in the abdomen, or within the mediastinum, and intralobar sequestration most often occurs in the lower lobes [39–41].

Sequestration is often diagnosed on prenatal ultrasound. Fetal MR imaging may be performed to further characterize lesions, which typically demonstrates a lesion that is hyper-

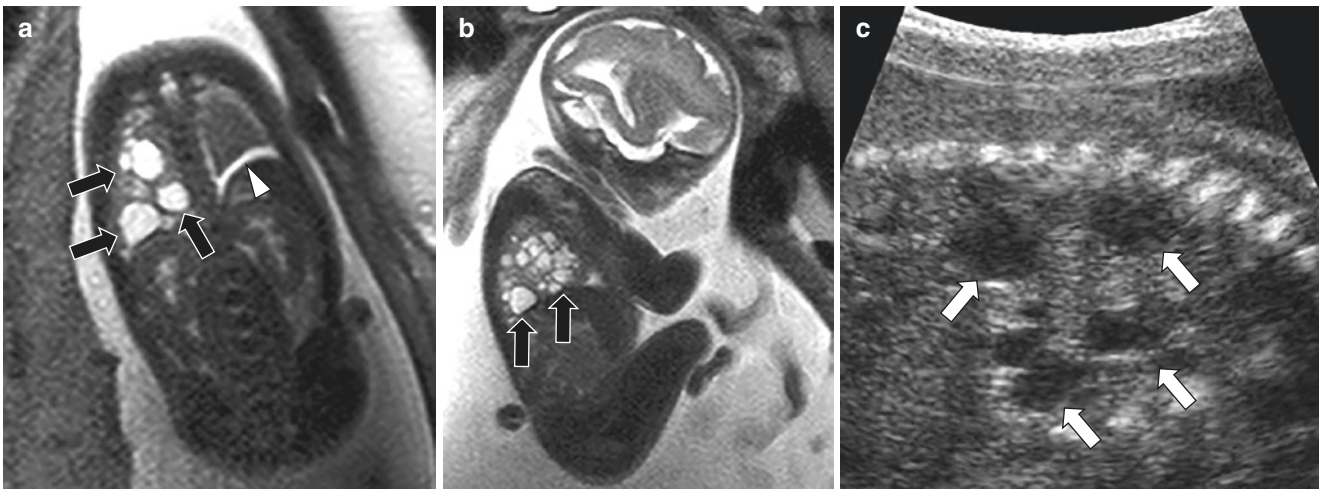

Fig. 1.11 Macrocystic congenital pulmonary airway malformation (CPAM) on prenatal MR imaging. (**a**) Coronal non-enhanced T2-weighted MR image shows several hyperintense cysts (*arrows*) in the right lung. A left pleural effusion (*arrowhead*) is also present. (**b**) Sagittal non-enhanced T2-weighted MR image shows several hyperintense cysts (*arrows*) in the lung. (**c**) Sagittal ultrasound image shows several hypoechoic cysts (*arrows*) in the lung

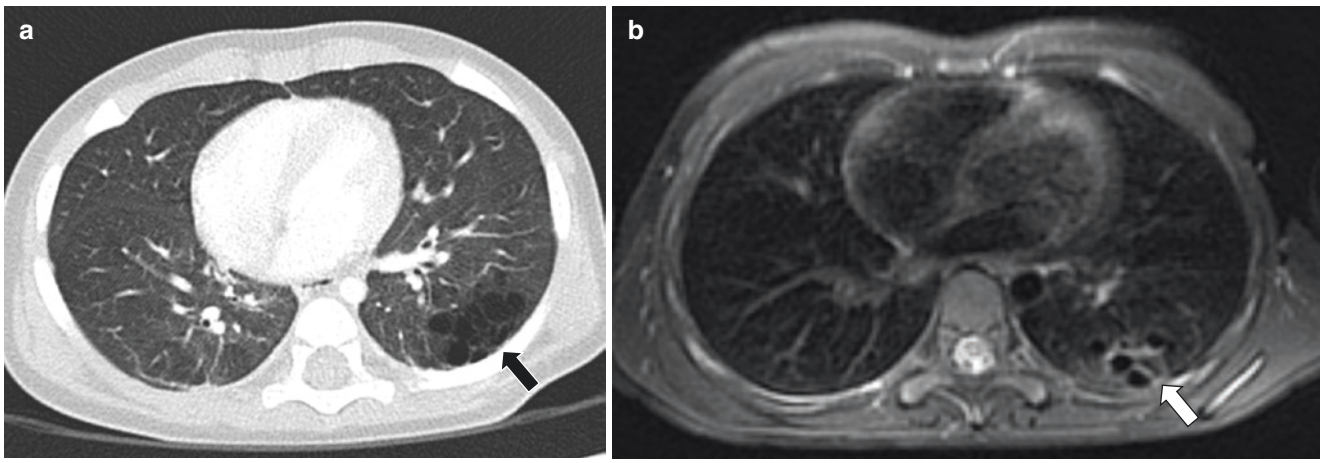

Fig. 1.12 Congenital pulmonary airway malformation (CPAM) type 2 in a boy at 7 months old and 9 years old. (**a**) Axial enhanced lung window setting CT image at 7 months of age shows multiple cysts (*arrow*) measuring <2 cm in the left lower lobe. (**b**) Axial enhanced T1-weighted fat-suppressed PROPELLER MR image at 9 years of age shows multiple cysts (*arrow*) measuring <2 cm in the left lower lobe

intense on T2-weighted images (Figs. 1.13 and 1.14). A flow-void might be seen arising from the aorta, indicating the systemic arterial supply, but this is often difficult to visualize. Therefore, the MR imaging appearance may be similar to other lesions including CPAM, bronchial atresia, and congenital lobar emphysema [48, 49, 57].

After birth, cross-sectional imaging is often indicated, especially when surgical resection is considered. CTA is most often performed for this indication given its excellent temporal and spatial resolution and ability to visualize anomalous vasculature. MRA may be appropriate in certain cases, such as if there is heightened concern about the effects of ionizing radiation. The key to imaging pulmonary sequestration is defining the arterial supply and the venous drainage. On conventional fluid-sensitive MR imaging sequences, sequestration typically appears as a cystic or solid lesion within the lung [31]. MRA demonstrates the systemic feeding artery (usually from the aorta) and the venous drainage to the left atrium (intralobar sequestration) or a systemic vein (extralobar sequestration) [31].

If symptomatic, pulmonary sequestration is treated with surgical resection. Similar to CPAM, management of asymptomatic pulmonary sequestration is somewhat controversial. Treatment may include resection due to concern about superinfection and small risk for malignancy or a watchful waiting strategy [58, 59].

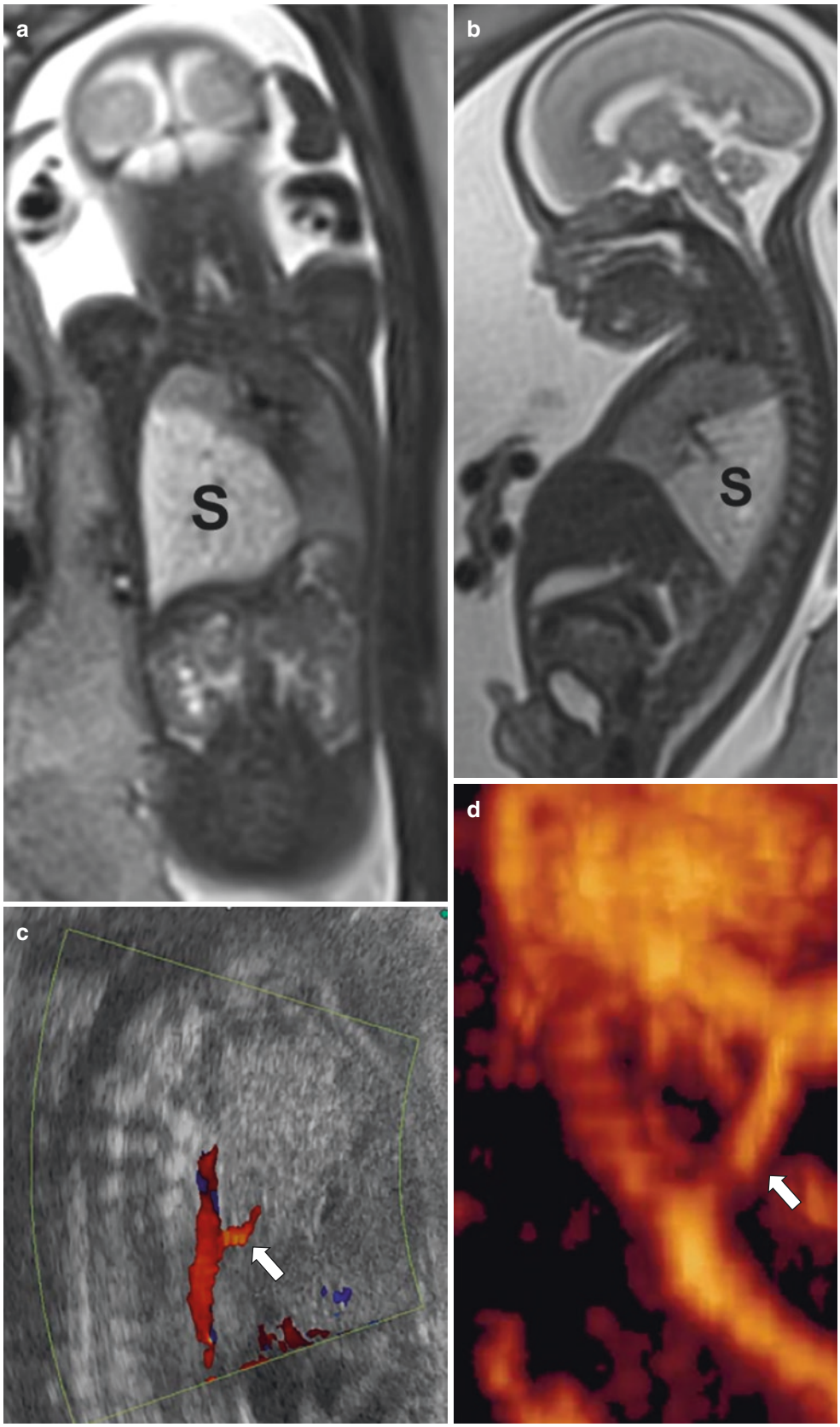

Fig. 1.13 Intralobar pulmonary sequestration on prenatal imaging. (**a**) Coronal non-enhanced T2-weighted MR image shows hyperintense lesion (S) replacing the right lower lobe and crossing the midline. (**b**) Sagittal non-enhanced T2-weighted MR image shows hyperintense lesion (S) replacing the right lower lobe. (**c**) Sagittal ultrasound image with color Doppler shows an anomalous systemic artery (*arrow*) arising from the descending thoracic aorta. (**d**) 3D reconstructed ultrasound image shows an anomalous systemic artery (*arrow*) arising from the descending thoracic aorta

Fig. 1.14 Extralobar infradiaphragmatic pulmonary sequestration on prenatal MR imaging. Coronal non-enhanced T2-weighted MR image shows hyperintense lesion (*arrow*) inferior to the left diaphragm

Infectious Lung and Pleural Disorders

Infections of the lungs and pleura are among the most common reasons for children to require medical attention [60, 61]. Imaging is often performed in these children, most commonly beginning with chest radiographs. When complicated infection is suspected, cross-sectional imaging tests are often performed, frequently CT. With increased concern about the potentially harmful effects of ionizing radiation, and technical advances allowing for diagnostic MR imaging imaging of the thorax, MR imaging has begun to gain attention as a potential alternative to CT in this scenario. A large number of different infections may affect the lungs and pleura, and there is overlap in the imaging features of different infections. In this section, the most frequently encountered pediatric infections of the lungs and pleura are described, and common MR imaging patterns of these infections are illustrated.

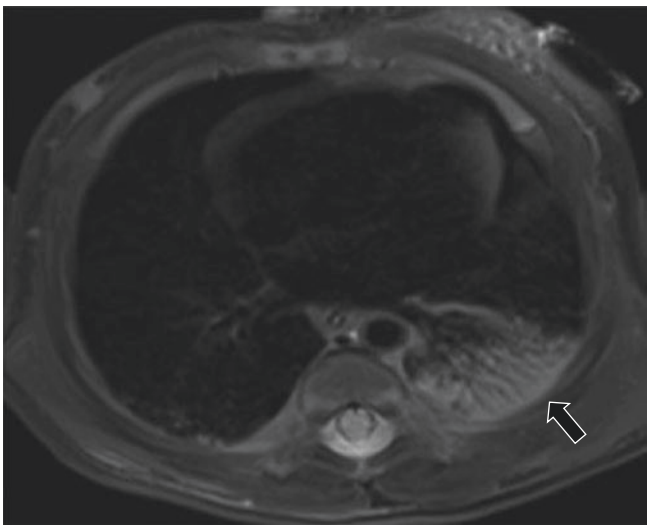

Fig. 1.15 Aspiration pneumonia in a 3-week-old girl who presented with fever and respiratory distress. Axial non-enhanced T2-weighted fat-suppressed MR image shows left lower lobe consolidation (*arrow*)

Bacterial Infection Bacterial infection of the lung causes pneumonia. Pleural effusion may occur in association with bacterial pneumonia, and empyema occurs if infection spreads to the pleural space. The two most common pathogens to cause bacterial pneumonia in the pediatric population are *Streptococcus Pneumoniae and Staphylococcus Aureus.* Less common pathogens include *Haemophilus Influenzae*, *Bordetella Pertussis*, and *Klebsiella Pneumoniae.* Other pathogens may occur in specific scenarios, for example, *Group B Streptococcus* infection in newborn children of colonized mothers, *Pseudomonas Aeruginosa* infection in pediatric patients with cystic fibrosis, and anaerobic organisms in aspiration pneumonia.

Three main patterns have been recognized in bacterial pneumonia. These include pulmonary consolidation, bronchopneumonia, and atypical pneumonia. Pulmonary consolidation occurs when alveoli fill with exudate, inflammatory cells, and fibrin (Fig. 1.15) [62]. In children consolidation may be lobar or spherical, resulting in "round pneumonia" [63, 64]. Bronchopneumonia describes a pulmonary infection characterized by peribronchial inflammation affecting multiple lobes and may result in patchy peribronchial consolidation and ground-glass signal (Fig. 1.16). Atypical pneumonia is a condition in which imaging may show only mild pulmonary findings such as mild reticular or patchy opacities without a focal region of consolidation, and symptoms may include headache and sore throat [65]. In current clinical practice, these three patterns are most often seen on chest radiograph or CT, but the findings may also be seen on MR imaging. Detailed descriptions of the specific MR imaging

findings (e.g., consolidation and ground-glass signal) are covered in a subsequent section.

Pleural effusion may occur in association with bacterial pneumonia and is called parapneumonic effusion (see Fig. 1.16). Empyema occurs when infection spreads to the pleural space, resulting in thickening and hyperemia of the pleural membranes, complex fluid within the pleural space, and loculated pockets of infected fluid. These findings may be appreciated on MR imaging and include hyperintense non-enhancing complex fluid within the pleural space and hyperenhancing thickened parietal and visceral pleura. Rarely, a condition called empyema necessitans can occur when empyema spreads from the pleural space to the chest wall (Fig. 1.17). Empyema necessitans is most often caused by *Actinomyces israelii* or *Mycobacterium tuberculosis* infection.

Viral Infection Viral respiratory infections include bronchiolitis and viral pneumonia and occur when airborne viruses infect the respiratory mucosa. Infection leads to bronchial wall thickening, inflammation, and mucous production. Mucous plugging and bronchial wall thickening often lead to air trapping and atelectasis. Pleural effusions may accompany viral lower respiratory tract infection. Although these imaging findings are more often described on chest radiograph and CT, the finding may also be appreciated on MR imaging (Fig. 1.18).

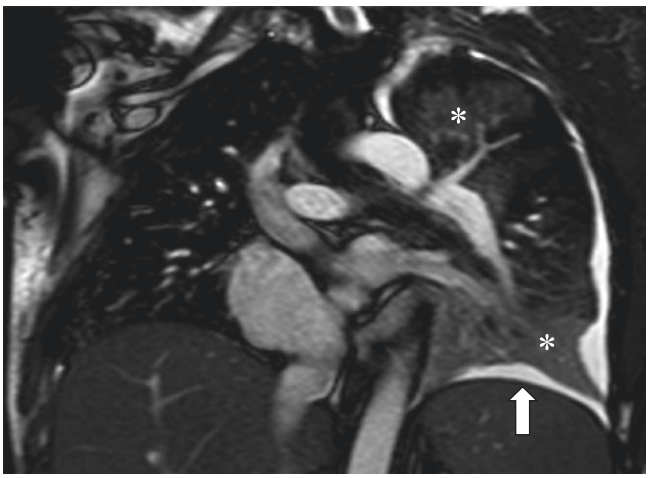

Fig. 1.16 Bacterial bronchopneumonia in a 16-year-old girl who presented with fever and cough. Coronal non-enhanced TruFISP/FIESTA MR image shows peribronchial ground-glass signal abnormality in the left upper and left lower lobes (*asterisks*) and a simple left pleural effusion (*arrow*)

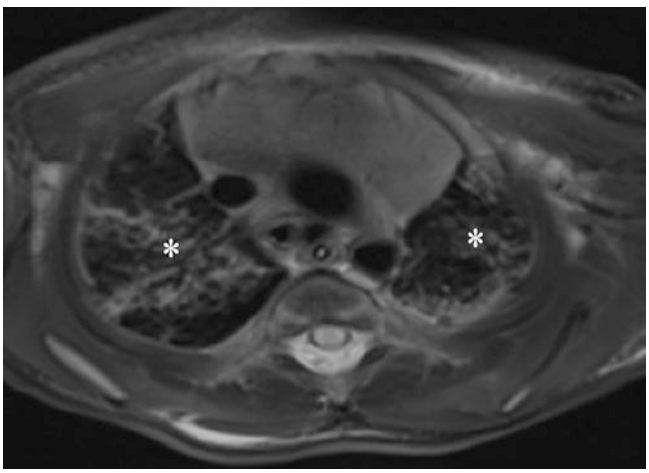

Fig. 1.18 Respiratory syncytial virus infection in a 1-week-old girl who presented with respiratory distress. Axial non-enhanced T2-weighted fat-suppressed MR image shows bilateral peribronchial interstitial thickening (*asterisks*)

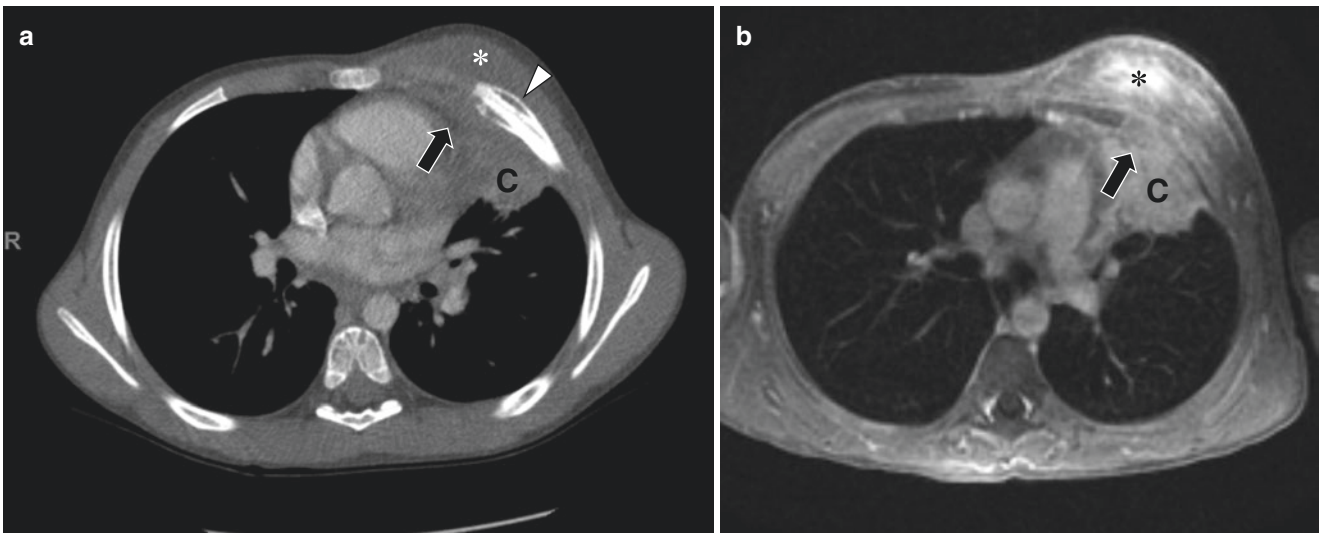

Fig. 1.17 Empyema necessitans in a 17-year-old boy who presented with fever and chest swelling. (**a**) Axial enhanced soft tissue window setting CT image shows consolidation (C) in the lingua, dense pleural fluid and soft tissue density (*arrow*), and left chest wall soft tissue thickening and inflammation (*asterisk*) with periosteal reaction (*arrowhead*) in the adjacent rib. (**b**) Axial enhanced T1-weighted fat-suppressed MR image shows consolidation (C) in the lingua, pleural soft tissue thickening (*arrow*), and left chest wall soft tissue thickening and inflammation (*asterisk*)

A large number of different viruses may cause lower respiratory tract infection in children. Respiratory syncytial virus (RSV) is the most common cause of viral bronchiolitis in infants and young children (see Fig. 1.18). Other viruses that may result in lower respiratory tract infection include human metapneumovirus, parainfluenza virus, rhinovirus, influenza, adenovirus, and cytomegalovirus, among others.

Fungal Infection Fungal infection of the lungs is uncommon in immunocompetent children but is relatively frequent in immunocompromised children [66]. The most common pulmonary fungal infections are aspergillosis, coccidioidomycosis, and histoplasmosis in the pediatric population. Pulmonary infection most often occurs when airborne fungi enter and disseminate through the lung via endobronchial spread, resulting in multiple pulmonary nodules distributed in a tree-in-bud pattern (Figs. 1.19 and 1.20) [65]. Hematogenous spread also occurs, leading to a pattern of small randomly distributed pulmonary nodules in a "miliary" pattern. Pulmonary nodules in fungal infection often

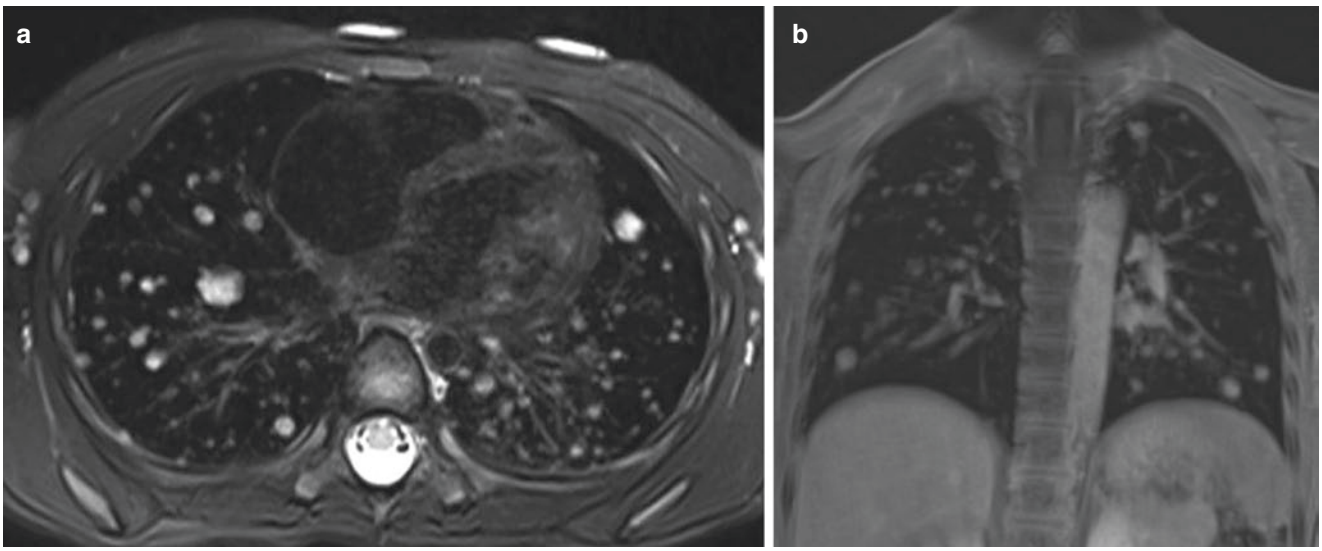

Fig. 1.19 Pulmonary coccidioidomycosis infection in a 5-year-old girl who presented with fever, cough, and headache. (**a**) Axial non-enhanced T2-weighted fat-suppressed MR image shows numerous bilateral hyperintense pulmonary nodules. (**b**) Coronal enhanced T1-weighted fat-suppressed MR image shows numerous bilateral hyperintense pulmonary nodules

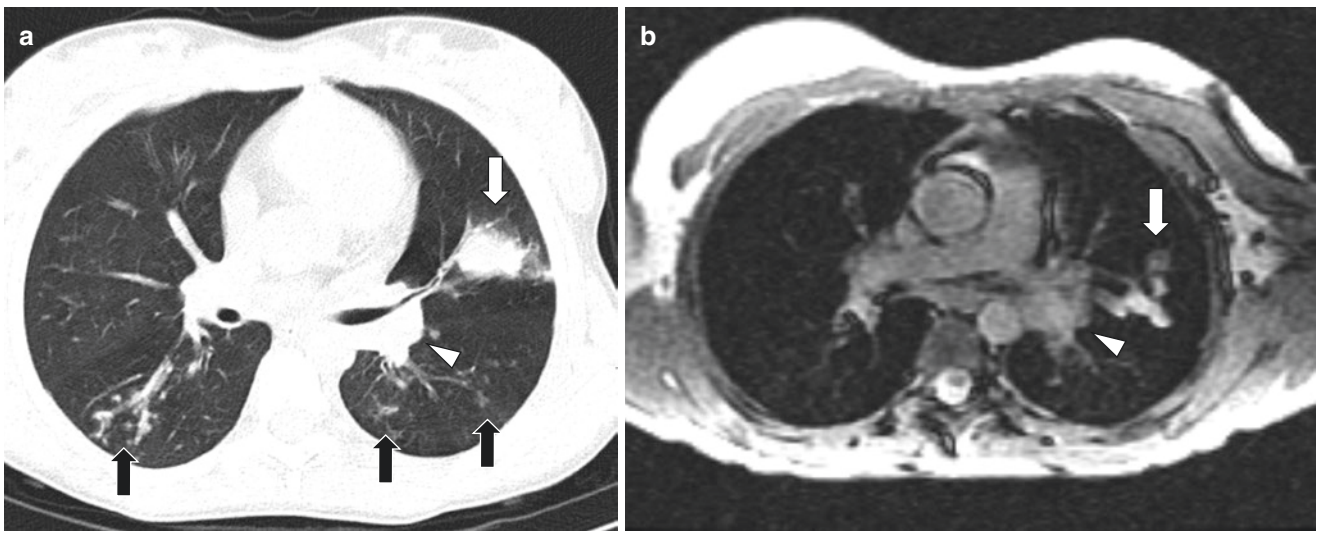

Fig. 1.20 Pulmonary *Aspergillus* infection in 14-year-old girl with cystic fibrosis. (**a**) Axial enhanced lung window setting CT image shows tree-in-bud nodularity (*black arrows*) in bilateral lower lobes, a larger nodule (*white arrow*) with ground-glass halo in the left upper lobe, and left hilar adenopathy (*arrowhead*). (**b**) Axial non-enhanced SSFP T2/T1-weighted MR image shows left upper lobe nodule (*arrow*) and left hilar adenopathy (*arrowhead*)

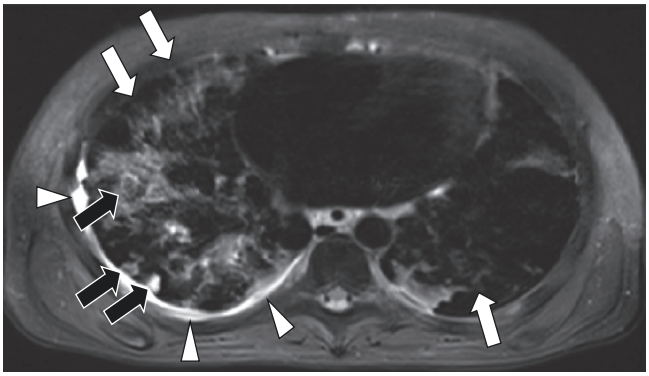

Fig. 1.21 Mycobacterium tuberculosis infection in 13-year-old boy with immunosuppression. Axial non-enhanced T2-weighted MR image shows multiple hyperintense and ground-glass pulmonary nodules (*black arrows*), bilateral interstitial thickening (*white arrows*), and small right pleural effusion (*arrowheads*)

have a solid center (which may cavitate) surrounded by a rim of ground-glass signal intensity, producing a "halo" sign [67]. These findings are most often described on chest radiograph and CT, but they can also be seen on MR imaging as described in a following section.

Mycobacterial Infection (Tuberculosis) In the developing world, tuberculosis (TB) continues to be a significant cause of community-acquired illness and, in the developed world, TB primarily affects patients who are immunocompromised or patients who emigrate from the developing world (Fig. 1.21) [68–70]. Although chest radiograph and CT are the most commonly used imaging modalities to assess TB infection, MR imaging may be considered in certain scenarios. For example, MR imaging may be utilized in immunocompromised pediatric patients receiving multiple imaging studies in order to mitigate exposure to ionizing radiation.

The most common primary mode of transmission for TB infection is through inhalation of infected droplets, and the initial infection is termed primary TB. In children, primary infection most often causes mild symptoms with no findings on imaging studies [71]. Less often, primary infection may cause more significant symptoms and be accompanied by mediastinal and hilar lymphadenopathy and pulmonary parenchymal opacity (see Fig. 1.21) [72, 73]. Lymphadenopathy is most often mild, but in a minority of cases, lymph nodes can become significantly enlarged and cause significant bronchial obstruction [74, 75]. Pleural effusion occurs in approximately 22% of children with primary TB infection (see Fig. 1.21) [76]. In primary infection, MR imaging may be normal or demonstrate pulmonary consolidation, pulmonary nodules, pleural effusion, or lymphadenopathy (see Fig. 1.21) [77, 78].

Dormant infection may become active at a time after primary infection, referred to as reactivation TB. Symptoms typically include fever, night sweats, productive cough, and hemoptysis. Imaging findings in reactivation TB typically include upper lobe consolidation with cavitation [79]. MR imaging may demonstrate upper lobe consolidation as a region of increased signal on fluid-sensitive sequences and show central necrosis as a region of relatively lower signal intensity within the consolidation [78].

Hematogenous spread of TB infection can lead to innumerable small nodules scattered throughout the lungs, liver, and spleen, termed miliary infection [73]. Young children and immunocompromised pediatric patients are at higher risk for miliary disease. In miliary infection, MR imaging shows innumerable 1–3 mm nodules within the lungs, liver, and spleen.

Parasitic Infection (e.g., Hydatid Disease) Pulmonary hydatid disease is caused by infection with *Echinococcus granulosus*, a parasite whose definitive host is the dog or other canids and intermediate host is sheep, goats, pigs, cattle, horses, or camels. Children may become infected by ingesting the eggs of the parasite located within feces of infected canids. After ingestion, the eggs hatch in the child's gastrointestinal tract and larvae enter the bloodstream. By hematogenous spread, larvae can then form cysts throughout the body; the two most common locations are the liver and the lung. Although most hydatid infections occur during childhood, the hydatid infection is often indolent, and affected patients may not present until adulthood [80]. Pulmonary hydatid disease is rare in many regions of the world, but, in endemic regions, it is a common differential diagnosis for a cystic lung lesion [81]. Hydatid cysts are composed of three layers (pericyst, laminated layer, and germinal layer) with membranes between them [82].

Pulmonary hydatid disease may first be detected on chest radiograph as a single (81%) or multiple (19%) round densities ranging in size from 1 to 20 cm [83–85]. On CT, these lesions demonstrate internal fluid density and a smooth wall that is higher density than fluid (Fig. 1.22). If cyst communicates with the airway an "air-crescent" sign may be seen and a "water lilly" sign may be seen when a collapsed endocyst floats within a cyst [85, 86]. MR imaging may help differentiate pulmonary hydatid disease from other cystic lung lesions by showing characteristic hypoin-

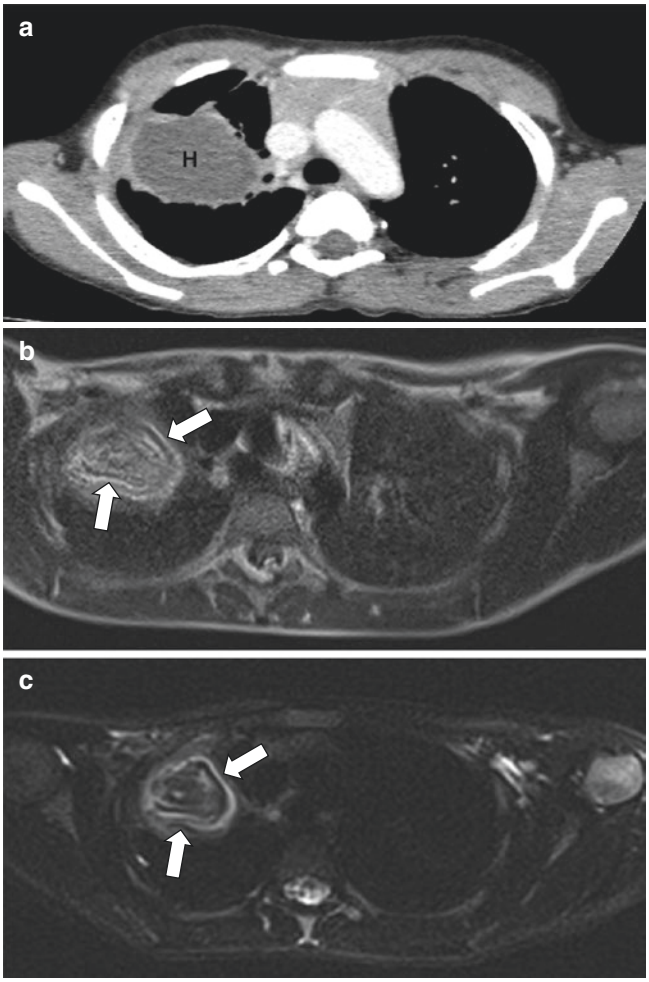

Fig. 1.22 Pulmonary hydatid disease in a 10-year-old boy who presented with chest pain and cough. (Courtesy of Kushaljit Singh Sodhi, MD, PhD, Department of Radiodiagnosis, Postgraduate Institute of Medical Education and Research, Chandigarh, India). (**a**) Axial enhanced soft tissue window setting CT image shows cystic lesion (H) with peripheral enhancement in the right upper lobe. (**b**) Axial non-enhanced T2-HASTE-weighted MR image shows internal folded membranes (*arrows*) within the cystic lesion. (**c**) Axial non-enhanced T2-BLADE-weighted MR image shows internal folded membranes (*arrows*) within the cystic lesion

tense folded membrane within the cyst and a hypointense rim surrounding the cyst (see Fig. 1.22) [81]. Recent prospective study which compared MR and contrast-enhanced MDCT for evaluation of pediatric pulmonary hydatid disease showed that fast MR imaging without contrast material is comparable to contrast-enhanced MDCT for accurately diagnosing lung cysts in pediatric patients with pulmonary hydatid disease. However, added diagnostic value demonstrating internal membranes of cysts, which is specific to pulmonary hydatid disease, was provided by MR imaging in comparison to MDCT [87].

MR imaging Findings of Infectious Disorders of the Lung and Pleura Pulmonary infection may produce a number of different findings on MR imaging. The following section illustrates these MR imaging findings.

Lung Consolidation Pulmonary consolidation is common in bacterial pneumonia. On CT, pulmonary consolidation appears as opacified lung which obscures pulmonary vessels, often with air bronchograms [88]. On MR imaging, homogenous signal intensity fills the normally hypointense lung and obscures pulmonary vessels (Fig. 1.23 and see Fig. 1.15) [88]. On T2-weighted sequences, the signal within pulmonary consolidation is typically greater than the signal in skeletal muscle. On contrast-enhanced T1-weigthed images with fat suppression, the region of consolidation typically enhances homogenously, unless there is necrosis.

Ground-Glass Signal Pulmonary infection may lead to ground-glass abnormalities within the lungs. On CT, ground-glass opacities are defined as opacities which are denser than the air-filled lung, but not dense enough to obscure the pulmonary vasculature. On MR imaging, ground-glass signal is defined as hyperintense signal within the lungs that is more intense than the air-filled lung

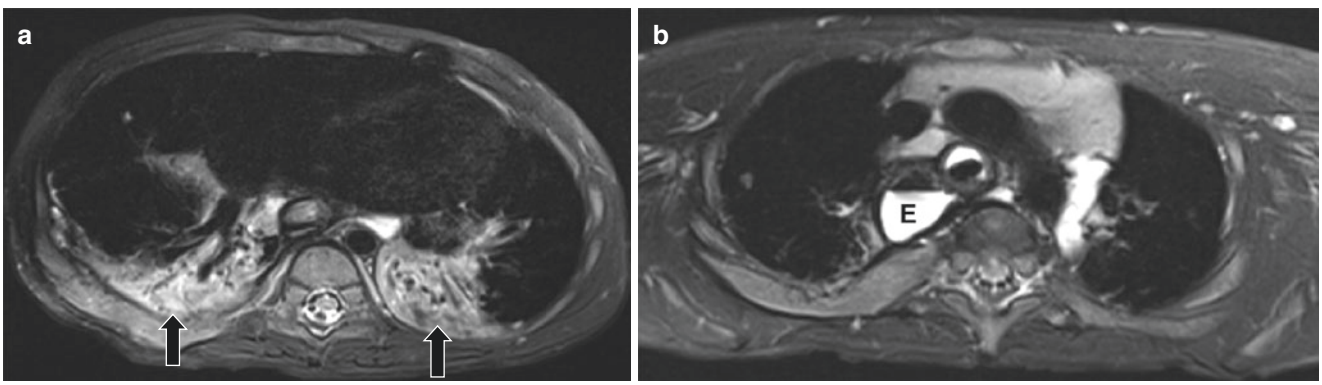

Fig. 1.23 Aspiration-related bilateral lower lobe consolidation in a 3-year-old boy with esophageal atresia repair. (**a**) Axial non-enhanced T2-weighted fat-suppressed MR image shows bilateral lower lobe consolidation (*arrows*). (**b**) Axial non-enhanced T2-weighted fat-suppressed MR image shows a dilated fluid-filled esophagus (E)